An enhanced inverted encoding model for neural reconstructions

Paul S. Scotti, Jiageng Chen, & Julie D. Golomb

Department of Psychology, The Ohio State University, Columbus, Ohio, USA

Please address correspondence to:
Paul S. Scotti
Email: scottibrain@gmail.com

Abstract word count: 146
Main text word count: 4,995
Figures: 4

Abstract

Here we present a more interpretable and flexible approach for reconstructing the contents of perception, attention, and memory from neuroimaging data. Our enhanced inverted encoding model (eIEM) incorporates methodological improvements including proper accounting of population-level tuning functions and a trial-by-trial prediction error-based metric where reconstruction quality is measured in meaningful units. Improved flexibility is further gained via eIEM's novel goodness-of-fit feature: for trial-by-trial reconstructions, goodness-of-fits are obtained independently (non-circularly) to prediction error and can be applied to any IEM procedure or decoding metric, resulting in improved reconstruction quality and brain-behavior correlations. We validate eIEM from methodological principles, simulated neuroimaging datasets, and three pre-existing fMRI datasets spanning perception, attention, and working memory. Notably, eIEM is easy to apply and broadly accessible – our Python package (https://pypi.org/project/inverted-encoding) implements eIEM in one line of code – and is easily modifiable to compare performance metrics and/or scale up to more complex models.

1. Introduction

A mental representation can be defined as the "systematic relationship between features of the natural world and the activity of neurons in the brain"[1]. An increasingly common approach to study mental representations using neuroimaging data is to employ encoding models, which describe this relationship computationally, typically by reducing the complexity of the input data with a set of functions that, when combined, roughly approximate the neural signal.

Encoding and decoding models (aka voxelwise modeling or stimulus-model based modeling) have become a standard method for investigating neural representational spaces and predicting stimulus-specific information from brain activity[2–4]. The key advantages of such models over other computational approaches such as multivariate pattern classification or representational similarity analysis are typically touted as the following: (1) Encoding models can take inspiration from single-unit physiology by consisting of tuning functions in stimulus space (aka feature space), allowing both the maximally receptive feature and the precision/sensitivity of the tuning to be estimated across a population of neurons. (2) Encoding models (which transform presented stimuli into predicted brain activity) are easily inverted into decoding models (which transform observed brain activity into predicted stimuli), and this process can be applied to a wide range of stimuli, including oriented Gabor patches[5,6], colors[7], acoustic musical features[8], and human faces[9]. (3) The decoding model can predict, or *reconstruct*, novel stimuli or experimental conditions not used in the training of the model, with reconstructions offering interpretational advantages beyond classification-based decoding by yielding measures of activity across the full stimulus space and

facilitating research questions exploring representational schemes for brain regions of interest[4,7].

The inverted encoding model (IEM) is one example of an encoding and decoding model that has quickly risen to prominence in the cognitive neuroscience community (see Supplemental Figure 1)[10–36]. The basic idea behind IEMs is illustrated in Figure 1A. First, an encoding model is trained to associate patterns of brain activity with specific stimuli. The model uses simple linear regression and a basis set representing the hypothesized population-level tuning functions, consisting of several channels that are modeled as cosines (or von Mises functions) equally separated across stimulus space (e.g., orientation, color, spatial location). Each channel in the basis set can be assigned a weight per voxel (we adopt fMRI nomenclature here, but IEMs can be applied to any modality like EEG, MEG, etc.) and hence a model can be trained to predict the activity of each voxel using the weights of each channel as predictors (i.e., the regressors in a linear regression). Then, this trained encoder is inverted such that it becomes a decoder capable of reconstructing a trial's stimulus when provided with a novel set of voxel activations (see Methods for mathematical implementation).

IEM is popular due to its simplicity, robust performance, and grounding in single-unit physiology principles. However, the standard implementation of IEM has some critical flaws and limitations. As discussed more below, it can produce misleading or difficult to interpret results, does not account for the shape of the basis channels (as recently pointed out in some high-profile debates in the literature[37–40]), and it lacks a measure of decoding uncertainty. Compounding matters, various approaches exist for

evaluating IEMs (Supplemental Figure 1) and often researchers report several decoding metrics due to ambiguity over which metric is best.

Here we present a new “enhanced inverted encoding modeling” (eIEM) approach that improves the interpretability of stimulus reconstructions, addresses some key issues inherent in the standard IEM procedure, and provides trial-by-trial stimulus predictions and goodness-of-fit estimates.

In essence, eIEM is a combination of several modifications and improvements (some previously employed, some novel) on the standard IEM procedure depicted in Figure 1. First, with eIEM, the core encoder and decoder steps described above (i.e., least-squares linear regression for estimating channel weights and responses, using a basis set of hypothesized population-level tuning functions) remain the same as standard IEM, but the encoding model is repeatedly fitted with slightly shifted basis sets such that subsequent reconstructions are in stimulus space rather than channel space. This “iterative shifting” of the basis set has been employed in a few previous papers[41–43], but it is not common practice. Iterative shifting allows for more accurate reconstructions spanning the full stimulus space (allowing the remaining eIEM steps to be optimally applied), and aids more generally in reducing interpretation flaws and bias associated with impoverished basis sets, as illustrated in Supplemental Figure 2.

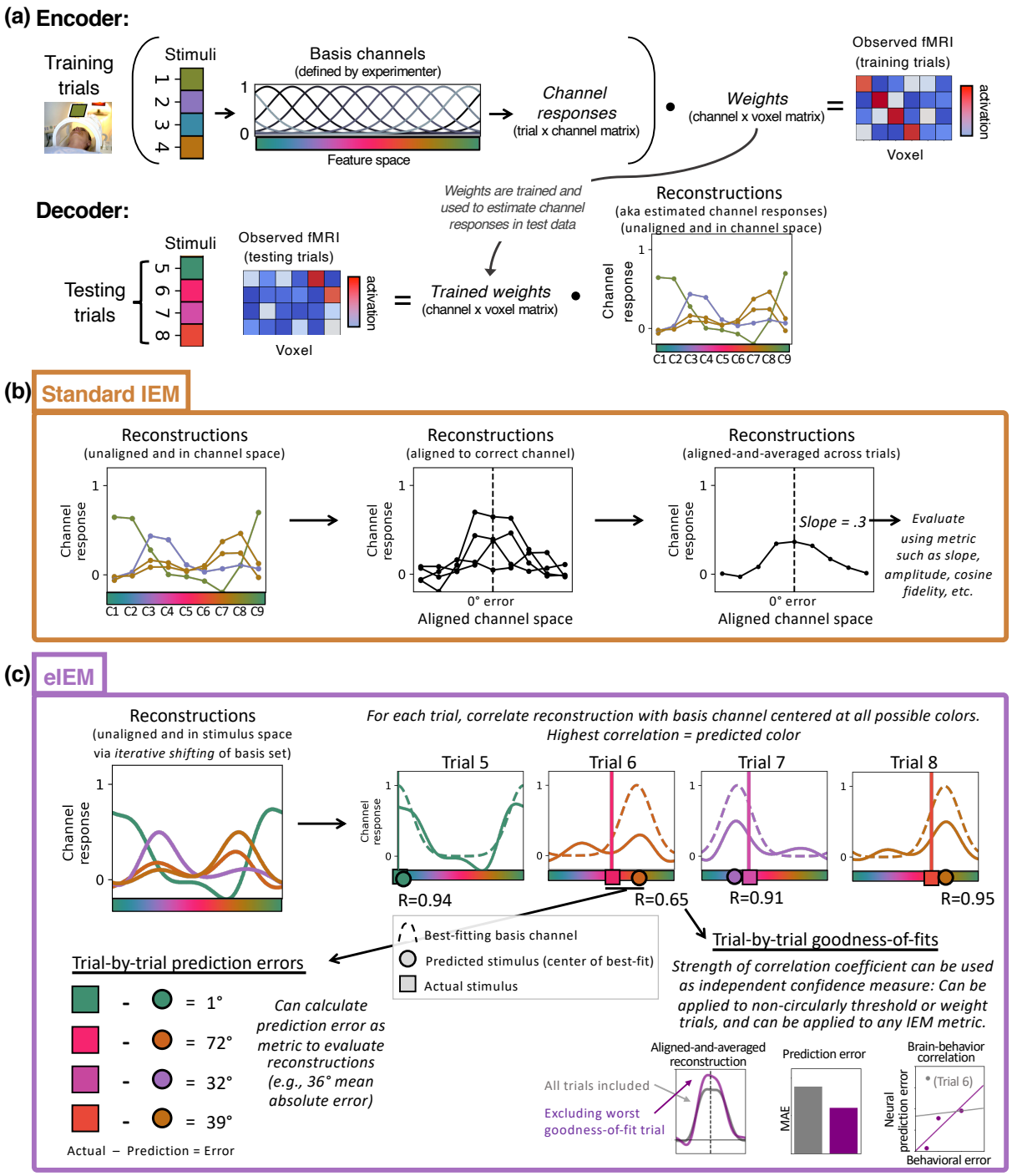

Figure 1. An overview of the steps involved in standard IEM and eIEM using a toy example of an fMRI experiment reconstructing stimulus colors. (a) Basic encoder and decoder steps common to both standard and eIEM. The prerequisites for implementing an IEM are the feature value of the stimulus for every trial (here 8 trials of colored squares), a trial-by-voxel matrix of brain activations for every voxel per trial (here simulated beta weights from a six-voxel brain region, and a basis set representing hypothesized population-level tuning functions; see Methods for details). The encoder models each voxel's response as the weighted sum of the

channels. Given that the trial-by-voxel matrix and the basis set are already given, the weights matrix can be estimated via least-squares linear regression. Once the weights matrix is estimated from the training dataset, it can be inverted such that the encoder becomes a decoder for the test dataset. Now, instead of estimating the weights matrix via least-squares linear regression, the weights matrix and the trial-by-voxel matrix are given and the channel responses (i.e., reconstructions) are estimated. The resulting estimated channel responses, or simply *reconstructions*, is a trial-by-channel matrix where each trial has its own reconstruction composed of weighted cosines. For simplicity, this example shows the encoder trained on the first half of trials and the decoder used to predict the color of the remaining trials, but in most applications cross-validation should be used such that every trial may be decoded while avoiding circularity/double-dipping. (b) The standard procedure involves aligning and averaging reconstructions and measuring the result according to a variety of possible metrics (e.g., amplitude, slope; see Supplemental Figure 1). (c) eIEM deviates from the standard procedure by evaluating trial-by-trial reconstructions rather than an averaged reconstruction. We use iterative shifting of the basis set to allow channel space to equal stimulus space, correlate the reconstructions with the full set of basis channels to estimate each trial's predicted stimulus (and then average prediction error), and also estimate goodness-of-fits for each trial's reconstruction.

More critically, the core difference of eIEM is that we analyze reconstructions at the trial-by-trial level, using a procedure that can obtain stimulus predictions, prediction error, and goodness-of-fits for each trial. In contrast, standard IEM typically employs an align-and-average approach (Figure 1B), where each trial's reconstruction is circularly shifted along the x-axis such that it is centered on the "correct" channel (closest to the ground truth stimulus feature), and then these aligned reconstructions are averaged together to result in a single reconstruction, typically quantified using metrics such as slope, amplitude, etc. As we show in the Results, this align-and-average approach is susceptible to information loss, outlier bias, and interpretation issues.

With eIEM, these aligned-and-averaged reconstructions can still be obtained for visualization purposes, but eIEM offers several novel advantages for evaluating, quantifying, and interpreting reconstructions. eIEM obtains trial-by-trial stimulus predictions using a correlation table approach (previously used in a small number of papers[7,42]) that adapts to the shape of the basis channel (Figure 1C). For each trial, a

set of correlation coefficients is computed, each reflecting the correlation between that trial's reconstruction and a basis channel (i.e., "perfect reconstruction") centered at every integer in stimulus space (e.g., resulting in 360 correlation coefficients for a stimulus space ranging from 0-359°). The highest of these correlation coefficients is determined to be the best fit for that trial, and the predicted stimulus feature for that trial is simply the center of that best-fitting basis channel. As described below in the Results, evaluating reconstructions using stimulus predictions obtained via this approach is more methodologically sound than, say, taking the location of highest amplitude as the stimulus prediction[25,44], because the shape of the basis functions is automatically taken into account.

To quantify reconstruction quality, eIEM naturally lends itself to prediction error based summary metrics. The difference between the predicted and actual stimulus feature is that trial's prediction error; this error can be averaged across trials to obtain mean absolute error (MAE), mean signed error, etc. Here we advocate for MAE as a default metric for evaluating reconstruction quality, because of its simplicity and grounding in meaningful units (average prediction error), particularly compared to standard IEM metrics such as slope, amplitude, reconstruction fidelity, etc which use arbitrary units. However, MAE is not a necessary component of eIEM; researchers could still employ other aspects of eIEM while adopting other metrics that best fit their research question.

The final and most novel advantage that eIEM offers is the automatic calculation of trial-by-trial goodness-of-fit values. Recall that each trial's stimulus prediction is determined as the center of the best-fitting basis function. Because this is calculated

independently of the actual correct stimulus, the goodness-of-fit values themselves (correlation coefficients) can also be recorded and optionally leveraged to estimate trial-by-trial confidence of predictions. Individual trials in a neuroimaging study can vary substantially in signal quality (driven by attentional fluctuations, alertness, head motion, scanner noise, etc.) but the standard IEM procedure does not incorporate uncertainty into decoding performance. The lack of uncertainty information has been noted in other contexts, with some recent alternatives to IEM proposed to incorporate uncertainty[45,46]. eIEM has the advantage of easily and automatically producing a trial-by-trial measure of prediction uncertainty within the IEM framework itself. This enhancement adds substantial flexibility to the IEM procedure. For example, as depicted in Figure 1C, goodness-of-fit can be used to set thresholds in a non-circular manner, such that less reliable trials are excluded from reconstructions. As we demonstrate in the Results using real and simulated fMRI datasets, goodness-of-fit thresholding can substantially increase statistical power and performance in versatile ways.

Researchers can easily implement eIEM on their own through our publicly available Python package (https://pypi.org/project/inverted-encoding; see Methods for more information). The value of eIEM is primarily in terms of evaluating IEM results: using both real and simulated data, we show below that eIEM is better than the standard IEM approach in terms of improved interpretability, flexibility, functionality, and robustness to methodological concerns.

2. Results

We first validate eIEM and demonstrate its practical advantages by implementing both standard IEM and eIEM on three real fMRI datasets[43,47,48] spanning the research topics of perception, attention, and memory. We then use simulated reconstructions to illustrate additional methodological issues and limitations with standard IEM that eIEM addresses. See the Methods for information regarding each dataset and how data were processed.

2.1 Validating eIEM on real fMRI data

First, as initial validation, we confirmed that across all three datasets eIEM replicated the overall pattern of results obtained with the standard procedure (Figure 2). For consistency, we reanalyzed all datasets ourselves using a standard IEM procedure with slope as the decoding metric, even if the original paper did not employ this exact same procedure. We chose slope as it is a commonly used decoding metric across IEM papers (see Supplemental Figure 1).

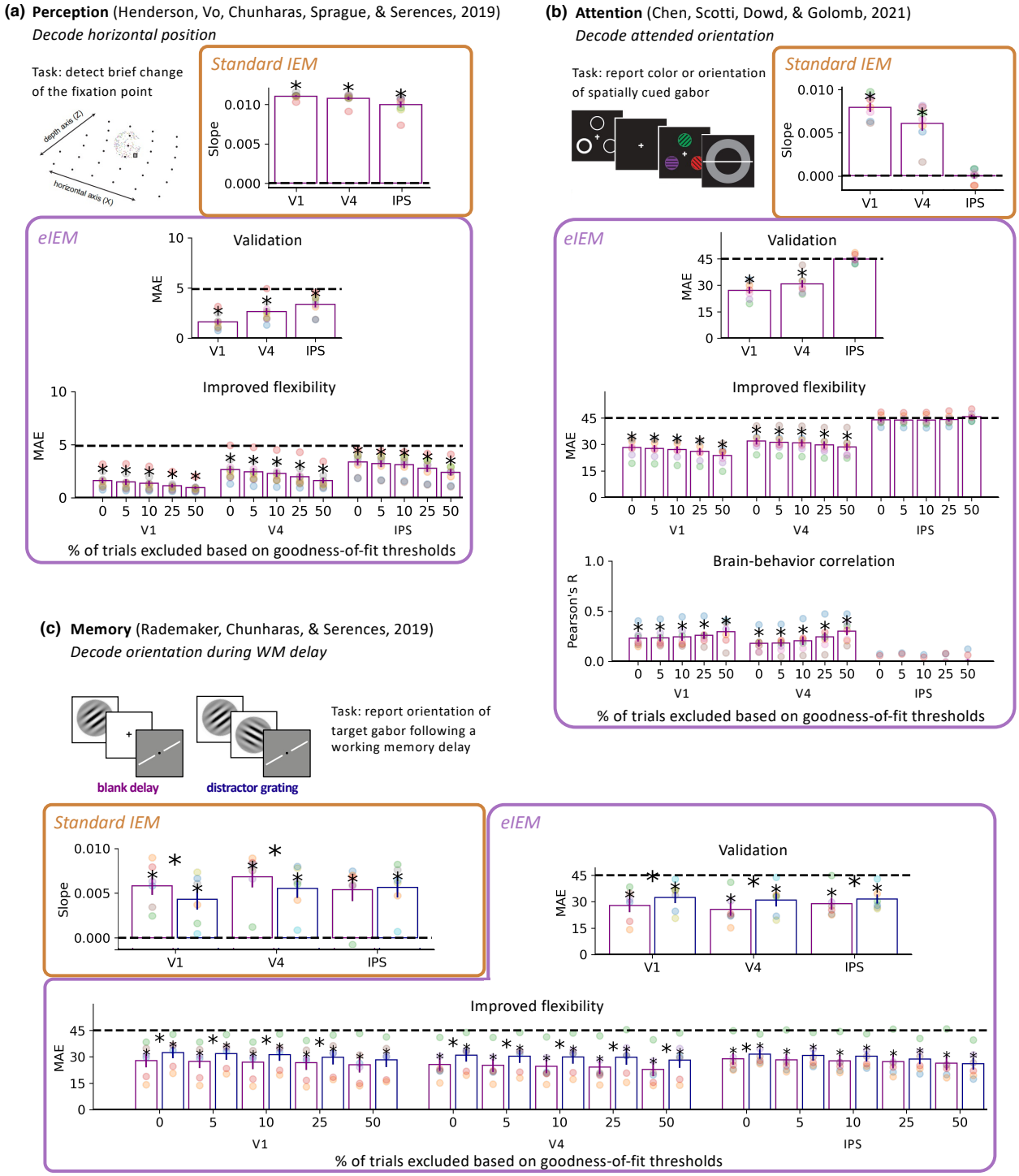

Figure 2. Results of the standard IEM procedure and our eIEM procedure across three real fMRI datasets spanning the topics of perception (a), attention (b), and memory (c). For each dataset, we show results obtained from the standard IEM procedure (orange boxes), our eIEM procedure without thresholding (purple boxes, 'Validation' plots), and eIEM using increasingly stringent cutoffs based on goodness-of-fit (purple boxes, 'Improved Flexibility' plots). Bar plots depict the reconstruction quality, using average slope for the standard procedure (higher values are better) and MAE for eIEM (lower values are better) across subjects, with individual subjects

overlaid as colored dots, for each of 3 ROIs (V1, V4, IPS). For the Attention dataset, the 'Brain-behavior correlation' plot additionally plots the trial-by-trial correlation between absolute behavioral error and absolute decoding error for each ROI and goodness-of-fit threshold. Error bars depict standard error of the mean, dotted black lines represent chance decoding, and asterisks represent statistically significant decoding ($p<.05$, no corrections for multiple comparisons). Overall results show that conclusions are similar between the standard IEM and eIEM, but MAE is more interpretable (not based in arbitrary units) and not prone to the methodological concerns we discuss later in the Results. In addition, each dataset showed that MAE consistently improved with increasing exclusion thresholds, demonstrating the flexibility of goodness-of-fit to exclude noisy trials. Increasing exclusion thresholds also appeared to strengthen brain-behavior correlations in the Attention dataset. See Supplementary Table 1 for test statistics and p values.

In the Perception dataset[48], we used both techniques to decode the horizontal position of a stimulus in V1, V4, and IPS. The standard procedure revealed significant decoding performance in all 3 ROIs, with the strongest decoding (greatest slope) in V1, followed by V4, and then IPS. eIEM replicated this pattern. In the Attention dataset[47], we used both techniques to decode the attended orientation within a multi-item, multi-feature stimulus array, in the same three ROIs. The standard IEM procedure revealed significant decoding in V1 and V4, but not IPS. eIEM again replicated this pattern. Finally, in the Memory dataset[43], we used both techniques to decode the remembered orientation of a stimulus over two types of working memory delays: blank delay and distractor delay. With the standard procedure, the remembered orientation was successfully decoded in V1, V4, and IPS, with significantly greater decoding in V1 and V4 during the blank delay compared to the distractor delay. With eIEM, we replicated each of those results, with the additional finding of significantly greater decoding during the blank vs distractor delay in IPS.

2.2 Demonstrating the improved interpretability and flexibility of eIEMs

Having validated our method across three diverse fMRI datasets, we next use these same datasets to illustrate the practical advantages of eIEM.

Improved interpretability. eIEM lends itself to metrics that are easily interpretable and comparable across datasets due to decoding performance being measured in terms of prediction error. In contrast, the arbitrary units of the standard aligned-and-averaged reconstructions are not easily interpretable. For example, in the Memory dataset, the standard procedure results in an average slope of .006 for the blank delay condition and .004 for the distractor delay condition in V1 (or cosine fidelity values of .100 and .098 as reported in the original paper[43]); eIEM replicates this pattern, but now with a more interpretable and meaningful metric: orientation can be decoded with an average error of 27.9 degrees in the blank delay and 32.5 degrees in the distractor condition. Note that the eIEM procedure does not have to use the MAE metric—e.g., if a researcher cares specifically about the amplitude of reconstructions then the eIEM framework can accommodate an amplitude-based metric (or whatever metric) that better aligns with the researcher's goals.

Incorporating trial-by-trial uncertainty. Next, we tested the flexibility of eIEM to make use of the trial-by-trial goodness-of-fit information. The eIEM approach produces a best-fitting stimulus prediction and associated goodness-of-fit value (correlation coefficient) for each trial. It is important to emphasize that the correlation coefficient reflects the degree to which the reconstruction matches the *best-fitting* basis channel, not the basis channel centered on the correct stimulus. In other words, this goodness-of-fit information is obtained without circularity. It is obtained independently and prior to any calculation of prediction error.

To test the impact of using goodness-of-fit information on decoding performance, we performed an analysis where we excluded trials with the lowest 5%, 10%, 25%, and 50% of goodness-of-fit values ("Improved flexibility" subplots of Figure 2). This resulted in visible improvements in MAE (i.e., smaller decoding error) with increasing exclusion thresholds for all three datasets (linear regression revealed significant negative slope in all cases except for IPS in the Attention dataset). Notably, in the Attention dataset, MAE improved with increasing thresholds in V1 and V4 (where decoding was significant in the unthresholded analysis) but not in IPS (where decoding was at chance in the unthresholded analysis). Thus, the goodness-of-fit information can be used to improve decoding performance when a brain region contains reliable information about a stimulus, but does not produce false positives in the absence of observable stimulus-specific brain activity.

This trial-by-trial prediction uncertainty information could be used in several ways. One suggestion we put forth is that goodness-of-fit can be used to threshold reconstructions, such that worse-fitting trials may be excluded from analysis. This principle is analogous to the phase-encoded retinotopic mapping and population receptive field modeling techniques, where a set of models spanning the full stimulus space is evaluated for every voxel, and the parameters of the best-fitting model are selected as that voxel's preferred stimulus, with the goodness-of-fit values then used to threshold the results[49–51]. Note that although r-squared is the more commonly used statistic for goodness-of-fit using regression, squaring the correlation coefficient is not preferred here because the sign of the correlation coefficient is informative (e.g., a perfectly inverted reconstruction should *not* be assigned equal confidence as a perfect

reconstruction), so we recommend the use of the r-statistic. Alternative approaches to trial thresholding also exist, including weighting trials based on their goodness-of-fit (see Discussion).

Goodness-of-fits obtained using eIEM can also be applied more broadly, beyond the MAE decoding metric. That is, one could use eIEM goodness-of-fits to threshold trials while using any of the commonly employed metrics of slope, amplitude, cosine fidelity, etc. Goodness-of-fit thresholding can also be applied directly to the reconstruction curves. We illustrate this point in Figure 3 using the above 3 fMRI datasets along with a simulated dataset. As increasingly strict goodness-of-fit thresholds were applied, the reconstruction curves were visibly improved. All of the quantification metrics similarly showed improvements with increasing goodness-of-fit thresholds. For the real fMRI datasets, these improvements generalized across all datasets, subjects (within-subjects and across-subjects), brain regions, and experimental conditions (mirroring the performance benefits shown in the “Increased flexibility” subplots of Figure 2). For the simulated dataset, these improvements generalized across the full range of simulation parameters tested, including number of trials, number of voxels, number and shape of basis channels, shape of voxel tuning functions, amount of noise,

etc, (code available to stimulate your own reconstructions on OSF:

https://osf.io/et7m2/).

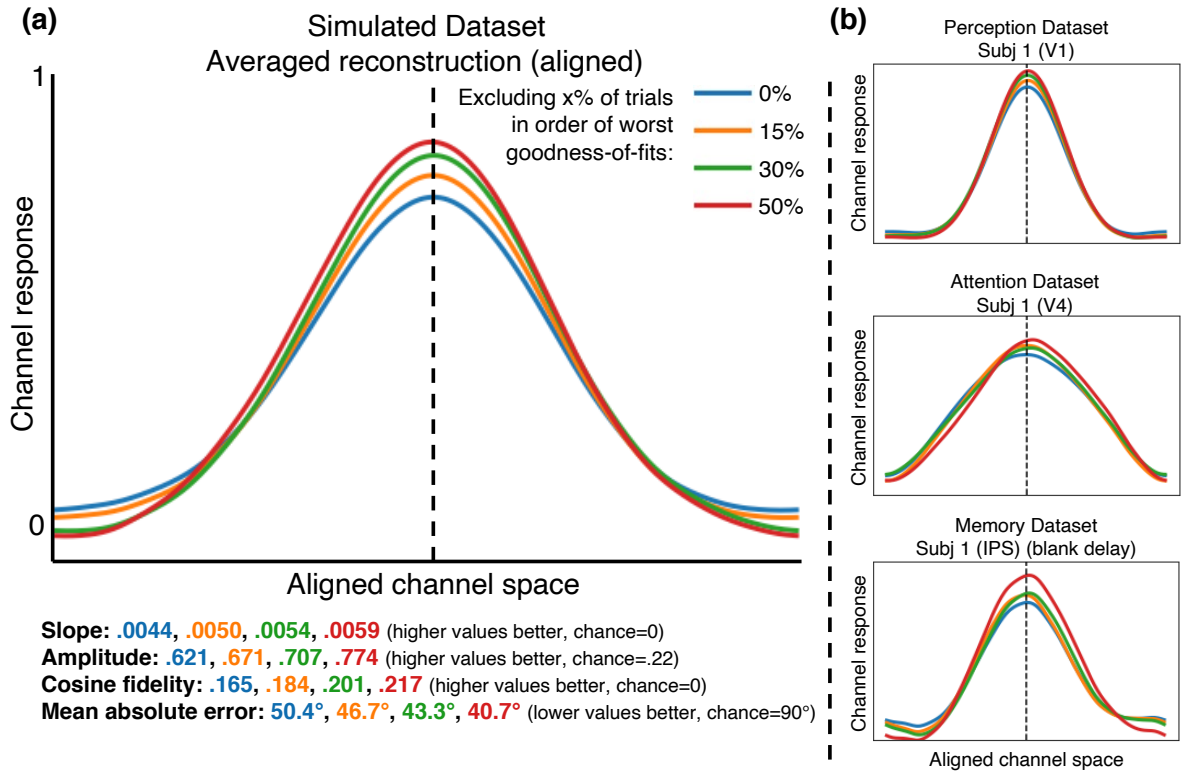

Figure 3. Simulated and real datasets show how eIEM goodness-of-fits can be applied to more traditional aspects of the standard IEM procedure. Different colors reflect different goodness-of-fit thresholds, implemented by exclusion of the X% worst fitting trials. Visual inspection of the reconstructions shows clear improvements with increasing thresholds. (a) Depiction shows the aligned-and-averaged reconstructions across 300 trials within a simulated brain region of 50 voxels, using a standard basis set of nine equally spaced channels. Several decoding metrics are shown below the curve, color-coded for each threshold level; all similarly benefitted from this trial thresholding, demonstrating the versatility of eIEM goodness-of-fits to benefit modeling outside of the eIEM framework. Results generalized across any simulation parameters tested; the code to reproduce these results and simulate reconstructions with varying parameters is available on OSF (https://osf.io/et7m2/). (b) We demonstrate the robustness of this approach to improve aligned-and-averaged reconstructions at the single-subject level across all three real fMRI datasets. Due to space limitations, we depict just three plots using the first subject of each dataset across three different ROIs, but this general pattern of stricter thresholds leading to improved reconstructions held across all datasets, subjects, brain regions, and experimental conditions.

Brain-behavior correlations. Finally, having trial-by-trial prediction error and goodness-of-fit values lends itself to analyses correlating neural measures with

behavior. We demonstrate this in the Attention dataset (the Perception dataset did not collect behavioral responses, and in the Memory dataset behavioral performance was too close to ceiling [~3° avg. error]). In V1 and V4, we observed a significant correlation between a trial's behavioral error magnitude and neural prediction error. Moreover, the strength of these correlations increased with higher goodness-of-fit thresholds ("Brain-behavior" subplot of Figure 2). We note that behavioral error itself did not noticeably change across these thresholds, suggesting that the goodness-of-fit information seemed to be reflecting noise at the level of the fMRI signal, not simply fluctuations in behavior or cognitive focus.

Altogether, these findings suggest that not only does eIEM produce more interpretable and robust results, but the trialwise goodness-of-fit values offer increased flexibility to improve both neural decoding power and brain-behavior correlations.

2.3 Additional methodological concerns addressed by eIEM

The three real fMRI datasets analyzed above are useful validation cases because they contain robust findings (as may be more likely with published, publicly available datasets), allowing us to convey the improved interpretability and flexibility of eIEM in cases where the overall pattern of decoding is consistent with standard IEM. Crucially, however, there are also cases where we would expect eIEM results to diverge from the standard IEM results due to various methodological concerns inherent in the standard approach. Below we illustrate some hypothetical cases susceptible to specific methodological concerns and limitations of the standard IEM procedure that are addressed by eIEM.

Standard IEM loses information from averaging across reconstructions.

Figure 4 depicts a few examples of how aligning and averaging reconstructions across trials could obscure important information. The hypothetical cases illustrated in panels 4a and 4b show one case where every trial is accurately reconstructed (i.e., centered on the correct stimulus feature with minimal error) and one case where every trial produces inaccurate reconstructions. These two cases would be interpreted identically according to standard IEM. In contrast, eIEM correctly identifies the first case as superior (lower MAE). Because eIEM evaluates prediction error on a trial-by-trial level and then averages the result, it avoids the pitfall of interpreting Figures 4a and 4b as reflecting the same quality of stimulus-specific brain signal.

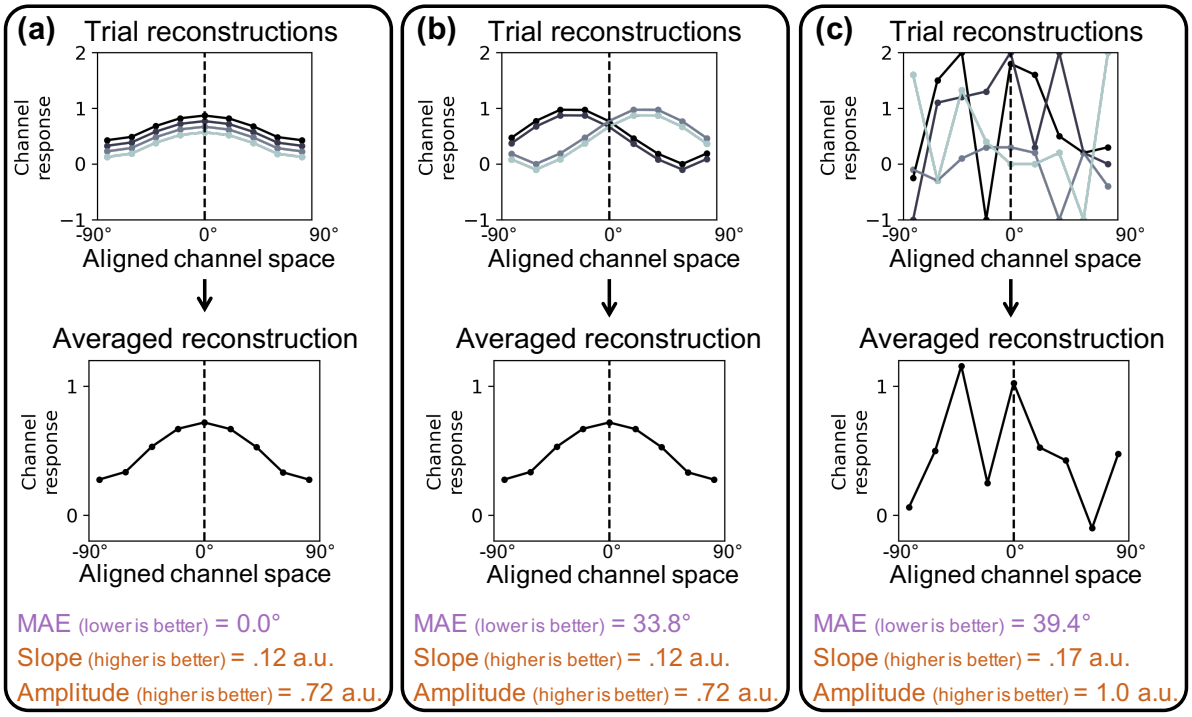

Figure 4. Visual depiction of how reconstructions with the standard procedure can produce spurious results because of not considering the variability of trial reconstructions or the shape of the basis channel. For each of the 3 hypothetical examples, the top row depicts four single-trial

reconstructions, and the row below depicts the aligned-and-averaged reconstruction. In (a) each individual trial's reconstruction accurately predicts the correct channel (i.e., the correct stimulus feature), appropriately reflected in the averaged reconstruction. In (b) each individual trial's reconstruction predicts an incorrect channel. Averaging across trials leads to a misleading result, i.e., the standard approach would consider (b) to reflect the same level of decoding performance as (a). In (c) each individual trial's reconstruction is essentially noise, such that the averaged reconstruction results in a false peak around the aligned point; the standard procedure using align-and-average metrics results in spuriously superior decoding performance than both (a) and (b), with (c) having a higher amplitude, steeper slope, and narrower standard deviation when fit with a gaussian distribution. The eIEM procedure, calculating MAE from trial-wise prediction error, correctly concludes that case (a) shows the best decoding performance.

Another advantage of eIEM is that MAE is also less prone to bias from outlier trials compared to any of the align-and-average metrics. In the standard IEM procedure, a single outlier reconstruction can disproportionately bias the shape of the averaged reconstruction, potentially completely flipping the averaged reconstruction in the most extreme cases. In contrast, the influence of an outlier is naturally capped for eIEM: Consider a hypothetical experiment composed of 300 trials where 299 trials predict the correct stimulus and one trial predicts the stimulus 180° away (assuming 360° stimulus space); because prediction error is calculated at the trial level and then averaged, an outlier trial could only increase MAE by a maximum 0.6°.

In addition to providing preferred solutions to the potential concerns of outlier bias and information loss, there are added advantages to evaluating trialwise reconstructions using eIEM, including increased versatility. For instance, our trialwise goodness-of-fit metric allows the researcher to predict which trials will likely produce better reconstructions (and hence better stimulus predictions). Complementary examples for how trialwise decoding metrics can allow increased flexibility in analysis include using trial-by-trial decoding error to help extract top-down spatial signals[44] or to correlate trial-by-trial decoding with memory-guided behavior across trials[24]. Critically,

eIEM's approach to calculating trialwise predictions avoids another known issue with the standard approach, as described below.

Standard IEM metrics wrongly assume a monotonic relationship between decoding performance and neural signal. As has been recently highlighted in the literature, IEMs produce reconstructions that depend on the choice of basis set[38,39]. Because the standard IEM procedure does not explicitly take this observation into account, this can result in faulty interpretations. Supplemental Figure 2 illustrates a rudimentary example of this issue that can be addressed with iterative shifting, but a more fundamental problem remains. That is, intuition – and standard practice – wrongly assume that a monotonic relationship exists between reconstruction quality measured by metrics such as slope, amplitude, and bandwidth, and the amount of stimulus-specific information in the brain signal. However, if the basis set consists of equally spaced and identical basis channels (which is typically the case)[a], then a "perfect" reconstruction returns the exact shape of the basis channel. Yet, the standard IEM approach can produce reconstructions from noisy neural data that appear *better* than this "perfect" benchmark. We argue that it makes more sense to directly compare the shape of the reconstruction to the shape of the basis channel to make predictions and evaluations. The correlation table metric employed in eIEM automatically adjusts to consider the shape of the basis channel because it is the basis channel itself that is

[a] If basis channels are not identical or are unequally shaped, one can simulate what a perfect reconstruction looks like at each stimulus feature and use these tuning functions in the same manner as the correlation table approach.

being used to obtain predictions, providing a more direct relationship between IEM performance and stimulus-specific brain signal.

Simply put, amplitude, slope, bandwidth, cosine fidelity, etc. are inferior metrics compared to the correlation table metric because they do not adapt to the choice of basis set. This is true even if a researcher were to skip the align-and-average step by evaluating reconstructions at the trial-by-trial level. For instance, using the amplitude metric, a higher amplitude at the aligned point is thought to reflect improved performance. If the basis channel ranges from 0 to 1, a perfect reconstruction should have an amplitude of exactly 1 at the aligned point, but reconstructions can feasibly have amplitudes far greater than 1. Likewise, the cosine fidelity (aka vector mean) approach of evaluating reconstructions by taking the dot product of the reconstruction and a standard cosine function could favor reconstructions with a wider width than expected under ideal conditions. Figure 4C illustrates an extreme example of this problem, where standard IEM metrics would produce spuriously high values, potentially leading one to falsely interpret the neural signal from Figure 4C as producing a better reconstruction than the signal from Figure 4A.

It is possible to partially account for the shape of the basis channel by, for example, fitting the reconstruction with a gaussian distribution (e.g., Henderson et al., 2019). However, such fitting procedures may be problematic because it forces the reconstruction to appear to be a reasonable gaussian shape regardless of the data (e.g., fitting Figure 4c with a gaussian distribution would still lead to the same incorrect conclusion of superior decoding performance compared to Figure 4a).

3. Discussion

Inverted encoding modeling has become a popular method for predicting stimuli and investigating neural representations because of its robust performance, simplicity of linear modeling, ability to predict untrained classes, and grounding in single-unit physiology. Our new eIEM technique improves the flexibility and interpretability of results while fixing important methodological concerns surrounding the standard IEM procedure. Namely, eIEM improves over standard IEM due to the following modifications: (1) iterative shifting of the basis channel returns reconstructions in stimulus space rather than impoverished channel space, (2) evaluating in meaningful units when decoding stimulus features improves interpretability and allows comparison of decoding performance across different model specifications, (3) calculating goodness-of-fits independently from stimulus predictions allows a trial-by-trial uncertainty measure that can be used to flexibly improve reconstruction quality and applications, (4) evaluating trial-by-trial stimulus reconstructions rather than the averaged reconstruction reduces information loss and outlier bias, and (5) evaluating reconstruction quality using the same tuning function used to build the encoder is more theoretically sound than assuming a monotonic relationship between reconstruction shape and neural signal. As demonstrated in the Results, this collective eIEM procedure offers both practical and in-principle benefits over the standardly adopted IEM. It is worth noting that while some prior papers have presented alternative IEM procedures that implement some of the modifications above, eIEM is unique in terms of its comprehensiveness and accessibility/simplicity. Moreover, the eIEM procedure is flexible: while our default eIEM procedure can be executed with a single line of code

from our openly available software package, this code can be also modified to selectively adopt aspects of the eIEM pipeline while customizing others. For example, a researcher may specifically care about the amplitudes of reconstructions rather than prediction error, so they may prefer to adopt all the above modifications except for evaluating in meaningful units. Alternatively, a researcher could customize the basis sets or other model parameters to test more advanced questions.

We validated the above advantages of eIEM using three fMRI datasets. Our validations demonstrated how our eIEM approach can be applied to both circular and non-circular stimulus spaces, is sensitive to variations in decoding performance across brain regions and experimental conditions, can be used to accurately decode the contents of perception, attention, and working memory, and can be used to meaningfully link neural reconstructions with behavior. Our modifications allowed for the decoding performance of each dataset to be directly compared to each other and demonstrated how uncertainty, measured via goodness-of-fit, can be leveraged to increase statistical power. Note that just because these three datasets produced consistent overall results (in terms of significance testing) across procedures does not ensure this will always be the case—for less reliable datasets with noisier underlying neural signals, the methodological pitfalls of standard IEM can become increasingly problematic.

One of the more novel aspects of eIEM is that researchers have the flexibility to exclude trials with noisier reconstructions based on our goodness-of-fit scores, which reflect how similar in shape each reconstruction is to the basis channel at the predicted stimulus. This flexibility can be used alongside *any* computational model or evaluation

metric because researchers could first threshold trials using goodness-of-fits obtained from our eIEM approach before proceeding to implement non-eIEM steps. A core difference between goodness-of-fits obtained using eIEM compared to standard IEM metrics that evaluate the shape of a reconstruction is that eIEM goodness-of-fits are obtained independently from prediction error—they are obtained without reference to the correct, ground truth stimulus (other metrics first center reconstructions at the correct stimulus and then evaluate the result, which is circular if used for trial thresholding). Note that we do not prescribe a specific cutoff for determining goodness-of-fit thresholds in this paper, rather, we simply offer that such an approach is possible for improving IEM performance. For example, a researcher could a priori decide to more heavily weight trials with higher confidences or simply exclude the noisiest 20% of trials.

Our method also improves interpretability by evaluating reconstructions in terms of prediction error. For example, “V1 showed 10° average prediction error and V4 showed 20° average prediction error” is more interpretable than “V1 showed .02 amplitude and V4 showed .01 amplitude” because the latter is in arbitrary units, whereas MAE is in meaningful units. Further, unlike amplitude or slope, the magnitude of prediction error is not dependent on the choice of basis set and can be directly compared to other experiments using the same stimulus space. This allows researchers to compare the quality of decoding across experiments or experimental conditions with differing model specifications.

In this paper we have referred to IEMs as a specific kind of encoding and decoding model that involves simple linear regression with population-level tuning functions. An advantage of eIEM is that improvements are accomplished without

sacrificing this simplicity—the encoding model weights and the decoding model channel responses are simply estimated via least-squares estimation. There are more complex neuroimaging methods that can similarly be used to produce reconstructions via hypothesized tuning functions. For instance, Kay et al., (2008) decoded natural images from brain activity via voxel-level receptive field models that describe tuning functions across space, orientation, and spatial frequency. Naselaris et al. (2009) further produced Bayesian reconstructions of natural images via the combination of encoding models meant to estimate structural and semantic content. Van Bergen and colleagues[46,52,53] introduced models where voxels with similar tuning account for shared noise and which produce trial-by-trial probability distributions such that uncertainty can be obtained similarly to our procedure (although the researchers discuss this in terms of testing Bayesian theories of neural computation rather than trial thresholding). Further work will be necessary to compare all these approaches, and we acknowledge that these more complex modeling approaches may be more useful than eIEM depending on the research question and the extent to which the researcher prefers model complexity over simplicity. For now, given the ample and broad interest in the cognitive neuroscience community towards implementing relatively more simplistic IEM procedures, we offer eIEM as an accessible means to improve reconstructions within the same familiar framework already popularized by IEM.

In summary, inverted encoding modeling has become increasingly popular in recent years, and yet the proper method for evaluating and interpreting IEMs has become increasingly uncertain. Our eIEM method is advantageous for both theoretical and practical reasons. From theoretical principles, we argue that eIEM is less

susceptible to methodological and interpretational pitfalls associated with standard IEM. We also demonstrate clear and practical advantages for evaluating reconstructions according to our eIEM method: as validated with real fMRI datasets, researchers can use eIEM to obtain improved reconstructions via thresholding with goodness-of-fits, compare decoding performance across varying basis sets using a metric grounded in meaningful units, evaluate performance in stimulus space rather than impoverished channel space, and obtain concrete stimulus predictions (with corresponding goodness-of-fits) for every trial rather than rely on a summary statistic based in arbitrary units. While there already exist approaches capable of addressing some of these concerns, our approach represents a suite of best practices that can be adopted by researchers in future work. Our procedure can be easily implemented with just one line of code using our accessible Python package (https://pypi.org/project/inverted-encoding; see Methods), and can be applied to investigate a vast range of research questions that involve reconstructing the contents of perception, attention, and memory from neuroimaging data.

Funding

This work was funded by the National Institutes of Health (R01-EY025648 to JDG) and the National Science Foundation (NSF DGE-1343012 to PSS, NSF BCS-1848939 to JDG).

References

1. Poldrack, R. A. The physics of representation. *Synthese* 1–19 (2020).
2. Naselaris, T., Kay, K. N., Nishimoto, S. & Gallant, J. L. Encoding and decoding in fMRI. *Neuroimage* **56**, 400–410 (2011).
3. Naselaris, T. & Kay, K. N. Resolving ambiguities of MVPA using explicit models of representation. *Trends Cogn. Sci.* **19**, 551–554 (2015).
4. Popov, V., Ostarek, M. & Tenison, C. Practices and pitfalls in inferring neural representations. *NeuroImage* **174**, 340–351 (2018).
5. Kay, K. N., Naselaris, T., Prenger, R. J. & Gallant, J. L. Identifying natural images from human brain activity. *Nature* **452**, 352–355 (2008).
6. Naselaris, T., Prenger, R. J., Kay, K. N., Oliver, M. & Gallant, J. L. Bayesian reconstruction of natural images from human brain activity. *Neuron* **63**, 902–915 (2009).
7. Brouwer, G. J. & Heeger, D. J. Decoding and reconstructing color from responses in human visual cortex. *J. Neurosci.* **29**, 13992–14003 (2009).
8. Casey, M., Thompson, J., Kang, O., Raizada, R. & Wheatley, T. Population codes representing musical timbre for high-level fMRI categorization of music genres. in *Machine Learning and Interpretation in Neuroimaging* 34–41 (Springer, 2012).

9. Lee, H. & Kuhl, B. A. Reconstructing perceived and retrieved faces from activity patterns in lateral parietal cortex. *J. Neurosci.* **36**, 6069–6082 (2016).
10. Ester, E. F., Anderson, D. E., Serences, J. T. & Awh, E. A neural measure of precision in visual working memory. *J. Cogn. Neurosci.* **25**, 754–761 (2013).
11. Ester, E. F., Sprague, T. C. & Serences, J. T. Parietal and frontal cortex encode stimulus-specific mnemonic representations during visual working memory. *Neuron* **87**, 893–905 (2015).
12. Ester, E. F., Sprague, T. C. & Serences, J. T. Categorical biases in human occipitoparietal cortex. *J. Neurosci.* **40**, 917–931 (2020).
13. Foster, J. J., Sutterer, D. W., Serences, J. T., Vogel, E. K. & Awh, E. Alpha-band oscillations enable spatially and temporally resolved tracking of covert spatial attention. *Psychol. Sci.* **28**, 929–941 (2017).
14. Foster, J. J., Bsales, E. M. & Awh, E. Covert spatial attention speeds target individuation. *J. Neurosci.* **40**, 2717–2726 (2020).
15. Garcia, J. O., Srinivasan, R. & Serences, J. T. Near-real-time feature-selective modulations in human cortex. *Curr. Biol.* **23**, 515–522 (2013).
16. Kok, P. & Turk-Browne, N. B. Associative prediction of visual shape in the hippocampus. *J. Neurosci.* **38**, 6888–6899 (2018).
17. Samaha, J., Sprague, T. C. & Postle, B. R. Decoding and reconstructing the focus of spatial attention from the topography of alpha-band oscillations. *J. Cogn. Neurosci.* **28**, 1090–1097 (2016).
18. Sprague, T. C. & Serences, J. T. Attention modulates spatial priority maps in the human occipital, parietal and frontal cortices. *Nat. Neurosci.* **16**, 1879–1887 (2013).

19. Sprague, T. C., Ester, E. F. & Serences, J. T. Reconstructions of information in visual spatial working memory degrade with memory load. *Curr. Biol.* **24**, 2174–2180 (2014).
20. Sprague, T. C., Ester, E. F. & Serences, J. T. Restoring latent visual working memory representations in human cortex. *Neuron* **91**, 694–707 (2016).
21. Yu, Q. & Shim, W. M. Temporal-order-based attentional priority modulates mnemonic representations in parietal and frontal cortices. *Cereb. Cortex* **29**, 3182–3192 (2019).
22. Cai, Y., Sheldon, A. D., Yu, Q. & Postle, B. R. Overlapping and distinct contributions of stimulus location and of spatial context to nonspatial visual short-term memory. *J. Neurophysiol.* **121**, 1222–1231 (2019).
23. Chen, N. *et al.* Sharpened cortical tuning and enhanced cortico-cortical communication contribute to the long-term neural mechanisms of visual motion perceptual learning. *Neuroimage* **115**, 17–29 (2015).
24. Hallenbeck, G. E., Sprague, T. C., Rahmati, M., Sreenivasan, K. K. & Curtis, C. E. Working memory representations in visual cortex mediate distraction effects. *Nat. Commun.* **12**, 4714 (2021).
25. Kok, P., Brouwer, G. J., van Gerven, M. A. & de Lange, F. P. Prior expectations bias sensory representations in visual cortex. *J. Neurosci.* **33**, 16275–16284 (2013).
26. Kok, P., Mostert, P. & De Lange, F. P. Prior expectations induce prestimulus sensory templates. *Proc. Natl. Acad. Sci.* **114**, 10473–10478 (2017).
27. Kok, P., Rait, L. I. & Turk-Browne, N. B. Content-based dissociation of hippocampal involvement in prediction. *J. Cogn. Neurosci.* **32**, 527–545 (2020).

28. Lorenc, E. S., Sreenivasan, K. K., Nee, D. E., Vandenbroucke, A. R. & D'Esposito, M. Flexible coding of visual working memory representations during distraction. *J. Neurosci.* **38**, 5267–5276 (2018).
29. Mostert, P. *et al.* Eye movement-related confounds in neural decoding of visual working memory representations. *Eneuro* **5**, (2018).
30. Oh, B.-I., Kim, Y.-J. & Kang, M.-S. Ensemble representations reveal distinct neural coding of visual working memory. *Nat. Commun.* **10**, 1–12 (2019).
31. Sprague, T. C., Itthipuripat, S., Vo, V. A. & Serences, J. T. Dissociable signatures of visual salience and behavioral relevance across attentional priority maps in human cortex. *J. Neurophysiol.* **119**, 2153–2165 (2018).
32. Sutterer, D. W., Foster, J. J., Adam, K. C., Vogel, E. K. & Awh, E. Item-specific delay activity demonstrates concurrent storage of multiple active neural representations in working memory. *PLoS Biol.* **17**, e3000239 (2019).
33. Tang, M. F., Arabzadeh, E. & Mattingley, J. B. Forward modelling reveals dynamics of neural orientation tuning to unconscious visual stimuli during binocular rivalry. *bioRxiv* (2019) doi:10.1101/574905.
34. Van Moorselaar, D. *et al.* Spatially selective alpha oscillations reveal moment-by-moment trade-offs between working memory and attention. *J. Cogn. Neurosci.* **30**, 256–266 (2018).
35. Vo, V. A., Sprague, T. C. & Serences, J. T. Spatial tuning shifts increase the discriminability and fidelity of population codes in visual cortex. *J. Neurosci.* **37**, 3386–3401 (2017).

36. Yu, Q., Teng, C. & Postle, B. R. Different states of priority recruit different neural representations in visual working memory. *PLoS Biol.* **18**, e3000769 (2020).

37. Gardner, J. L. & Liu, T. Inverted Encoding Models Reconstruct an Arbitrary Model Response, Not the Stimulus. *eNeuro* **6**, ENEURO.0363-18.2019 (2019).

38. Liu, T., Cable, D. & Gardner, J. L. Inverted encoding models of human population response conflate noise and neural tuning width. *J. Neurosci.* **38**, 398–408 (2018).

39. Sprague, T. C., Boynton, G. M. & Serences, J. T. The importance of considering model choices when interpreting results in computational neuroimaging. *Eneuro* **6**, (2019).

40. Sprague, T. C. *et al.* Inverted Encoding Models Assay Population-Level Stimulus Representations, Not Single-Unit Neural Tuning. *eNeuro* **5**, ENEURO.0098-18.2018 (2018).

41. Ho, T. *et al.* The optimality of sensory processing during the speed–accuracy tradeoff. *J. Neurosci.* **32**, 7992–8003 (2012).

42. Kim, I., Hong, S. W., Shevell, S. K. & Shim, W. M. Neural representations of perceptual color experience in the human ventral visual pathway. *Proc. Natl. Acad. Sci.* **117**, 13145–13150 (2020).

43. Rademaker, R. L., Chunharas, C. & Serences, J. T. Coexisting representations of sensory and mnemonic information in human visual cortex. *Nat. Neurosci.* **22**, 1336–1344 (2019).

44. Rahmati, M., Saber, G. T. & Curtis, C. E. Population Dynamics of Early Visual Cortex during Working Memory. *J. Cogn. Neurosci.* **30**, 219–233 (2018).

45. Li, H.-H., Sprague, T. C., Yoo, A., Ma, W. J. & Curtis, C. E. Joint representation of working memory and uncertainty in human cortex. *bioRxiv* (2021) doi:10.1101/2021.04.05.438511.

46. Van Bergen, R. S. & Jehee, J. F. TAFKAP: An improved method for probabilistic decoding of cortical activity. *bioRxiv* (2021) doi:10.1101/2021.03.04.433946.

47. Chen, J., Scotti, P. S., Dowd, E. W. & Golomb, J. D. Neural Representations of Task-relevant and Task-irrelevant Features of Attended Objects. *bioRxiv* (2021) doi:10.1101/2021.05.21.445168.

48. Henderson, M., Vo, V., Chunharas, C., Sprague, T. & Serences, J. Multivariate analysis of BOLD activation patterns recovers graded depth representations in human visual and parietal cortex. *Eneuro* **6**, (2019).

49. Dumoulin, S. O. & Wandell, B. A. Population receptive field estimates in human visual cortex. *Neuroimage* **39**, 647–660 (2008).

50. Engel, S. A., Glover, G. H. & Wandell, B. A. Retinotopic organization in human visual cortex and the spatial precision of functional MRI. *Cereb. Cortex N. Y. NY 1991* **7**, 181–192 (1997).

51. Sereno, M. I. *et al.* Borders of multiple visual areas in humans revealed by functional magnetic resonance imaging. *Science* **268**, 889–893 (1995).

52. Van Bergen, R. S. & Jehee, J. F. Modeling correlated noise is necessary to decode uncertainty. *Neuroimage* **180**, 78–87 (2018).

53. Van Bergen, R. S., Ma, W. J., Pratte, M. S. & Jehee, J. F. Sensory uncertainty decoded from visual cortex predicts behavior. *Nat. Neurosci.* **18**, 1728–1730 (2015).

54. Brouwer, G. J. & Heeger, D. J. Cross-orientation suppression in human visual cortex. *J. Neurophysiol.* **106**, 2108–2119 (2011).

55. Wandell, B. A., Dumoulin, S. O. & Brewer, A. A. Visual field maps in human cortex. *Neuron* **56**, 366–383 (2007).

56. Destrieux, C., Fischl, B., Dale, A. & Halgren, E. Automatic parcellation of human cortical gyri and sulci using standard anatomical nomenclature. *Neuroimage* **53**, 1–15 (2010).

57. Mumford, J. A., Turner, B. O., Ashby, F. G. & Poldrack, R. A. Deconvolving BOLD activation in event-related designs for multivoxel pattern classification analyses. *Neuroimage* **59**, 2636–2643 (2012).

Online Methods

We performed analyses on both real and simulated data. For the real fMRI datasets, we used two publicly available published datasets[43,48] and one unpublished dataset from our lab[47]. Note that we only analyzed a subset of the data from each dataset, analyzing one or two conditions across three brain regions for the sake of simplicity. The experimental paradigms and conditions / regions chosen are described more in each dataset's respective section below.

Inverted encoding model procedures

For all datasets, we performed a set of analyses using both the standard IEM and eIEM procedures (as depicted in Figure 1, with the exception that we used iterative

shifting for both the standard IEM and eIEM to facilitate more direct comparison). For both procedures, each basis channel was modeled as

$$\cos\left((\theta-\mu)\frac{\pi}{stimulus_range}\right)^{num_channels-1}$$

where θ is degrees in stimulus space, μ is the center of each channel, and *stimulus_range* is the range of stimulus space (e.g., 360° hues on a color wheel). The reasoning behind raising cosines to the *num_channels*-1 is to make the tuning curves narrower and more comparable to physiological findings [54]. For the encoder, each voxel's response was modeled as the weighted sum of the channels such that the observed trial-by-voxel fMRI activation matrix is equal to the dot product of the basis set and the weight matrix,

$$basis_set[trial_features,:]\cdot\ channel_by_voxel_weights = \ trial_by_voxel_activation$$

where *trial_features* is the feature (e.g., orientation) of the stimulus and *basis_set* is the matrix of channels with shape (*stimulus_range, num_channels*).

Once the weights matrix is estimated from the training dataset, it is inverted such that the weights matrix and the trial-by-voxel matrix are given and the channel responses (i.e., reconstructions) are estimated.

$$trial_by_voxel_activation\cdot\ channel_by_voxel_weights^{-1} = \ reconstructions$$

For all datasets, we used a basis set composed of nine equidistant channels each modeled as $\cos\left((\theta-\mu)\frac{\pi}{180}\right)^{8}$. We used 10-fold cross-validation, such that each iteration trained the model on 90% of the data and tested the model on the remaining 10%, repeated such that all trials were at one point decoded as part of the testing set.

For the standard IEM procedure, we aligned and averaged the single trial reconstructions into an average reconstruction and calculated slope as a traditional decoding metric. For the eIEM procedure, we calculated absolute prediction error for each trial via the correlation table metric and then calculated MAE. We performed these steps for each subject, ROI, and condition, and then we calculated the average slopes and MAEs across subjects.

For each condition and ROI, we assessed significance via permutation testing. Significance tests were one-sided and uncorrected, calculated by comparing the t-statistic calculated from the actual data against the permuted null distribution of t-statistics (one t-statistic per each of 5,000 permutations). For eIEMs, we also repeated this analysis pipeline using varying levels of goodness-of-fit thresholds. That is, we discarded a certain percent of trials based on the worst goodness-of-fits and then calculated MAE using the remaining trials. The full list of t-statistics and corresponding p-values for the tests performed in Figure 2 are displayed in Supplementary Table 1.

Perception dataset: Henderson, Vo, Chunharas, Sprague, and Serences (2019)

Data were obtained by downloading post-processed fMRI data associated with Henderson et al. (2019), publicly available on OSF (https://osf.io/j7tpf/). In this experiment, nine participants attended to a central fixation while a sphere (multicolored flickering dots positioned on the shell of a 3D sphere with radius 3.4°) was presented at varying positions along the horizontal and depth axes (depth achieved through stereoscopic MR-compatible goggles). The task was to detect a brief luminance change of the fixation point. Participants completed between 7 and 21 runs, where each run of

36 trials began with a sphere presented for 3s followed by a jittered intertrial interval (2-6s). There were also runs where participants covertly attended to the sphere, but we did not include these runs in the analysis. We only reconstructed horizontal position for simplicity and because position-in-depth was only sampled across six unique locations (varied sampling across the entire stimulus space is more appropriate for inverted encoding models) whereas horizontal position was sampled across 36 unique locations (from 0.9° to 9.8° eccentricity in both directions, collapsing across position-in-depth). We analyzed V1, V4, and IPS regions of interest which were defined via retinotopic mapping protocols where participants viewed rotating wedges and bowtie stimuli [55] while performing a covert attention task of detecting contrast dimming on a row of the checkerboard for the rotating wedge stimulus. We applied IEMs (following the procedures outlined earlier) to the post-processed data conducted by the authors of the original paper: Single-trial activation estimates consisted of averaged z-scored BOLD signal of the 3rd and 4th TRs following stimulus presentation. For more methods information, please refer to the original paper[48].

Attention dataset: Chen, Scotti, Dowd, & Golomb (2021)

Data were previously collected in our lab for another study Chen et al. (2021). In this experiment, seven participants completed a visual attention task. Each trial started with a central fixation cross. After 700ms, three circle outlines were displayed at equidistant locations surrounding the fixation cross for 200ms. One outline was thicker than the others, representing the spatial cue. Participants were instructed to covertly attend to the spatial cue location while maintaining fixation at the fixation cross. After

1100ms, three colored and oriented gratings were briefly displayed for 100ms, followed by a 200ms mask and a continuous orientation report. Participants were instructed to report the orientation of the grating that appeared at the location of the spatial cue. There were also trials where participants were asked to shift attention to a different spatial location before the onset of the gratings, and entire runs where participants were asked to attend and report the color of the grating (instead of orientation), but we did not include these in our analysis. Participants completed at least 440 trials of each condition across multiple runs and sessions. We analyzed V1, V4, and IPS regions of interest: V1 and V4 were defined via retinotopic mapping protocols where participants viewed rotating wedges and bowtie stimuli[55], while IPS was defined from the Destrieux atlas[56] in Freesurfer (parcel labelled “S_intrapariet_and_P_trans”). To obtain single-trial neural activations for IEM, we modified a commonly used single-trial general linear model (GLM) approach[57] to improve the model sensitivity and account for the large number of trials. Specifically, we conducted 40 GLMs per subject, where each GLM includes one regressor per run for one of the 40 trials in that run and one regressor per run for all the other remaining trials in that run. In this way, across the 40 GLMs, each trial in the experiment had an estimated single-trial beta weight. For more methods information, please refer to the original paper[47].

Memory dataset: Rademaker, Chunharas, and Serences (2019)

Data were obtained by downloading post-processed fMRI data publicly available on OSF (https://osf.io/dkx6y)[43]. We reanalyzed Experiment 1, where six participants underwent a visual working memory task. For each trial, a cue indicating the distractor

condition was shown for 1.4s, followed by a target grating shown for .5s where participants were instructed to memorize its orientation, followed by a 1s blank delay, and then an 11s delay where 3 possible distractor conditions were possible: blank delay, Fourier-filtered noise, or distractor grating of a pseudo-random orientation. Following an additional 1s blank delay, participants had 3s to report the orientation of the target grating, and finally a variable intertrial interval (3/5/8s). Each participant completed 108 trials per distractor condition. We only reconstructed the blank delay and distractor grating conditions for simplicity. We analyzed V1, V4, and IPS regions of interest which were defined via retinotopic mapping protocols where participants viewed rotating wedges and bowtie stimuli[55]. We applied IEMs to the post-processed data conducted by the authors of the original paper: Single-trial activation estimates consisted of averaged BOLD signal between 5.6-13.6s (7-17 TRs) after target onset. For more methods information, please refer to the original paper[43].

Simulated datasets

We used Python to simulate fMRI data from hypothetical brain region of interests with arbitrarily chosen numbers of voxels, where each voxel's ground truth tuning function was the same shape as the basis channel. For Figure 1 and Figure 3, we injected random noise from a gaussian distribution into the trial by voxel matrix to produce noisier data as would be expected from a real fMRI experiment. Simulated fMRI data were subjected to the IEM procedures described above to depict the contents of Figure 1, Figure 3, and Supplemental Figure 2. Our Jupyter notebook on OSF (https://osf.io/et7m2/) contains Python code to reproduce Figures 1 and 3, and can also

be used to simulate reconstructions with varying parameters including number of trials, number of voxels, number and shape of basis channels, shape of voxel tuning functions, amount of noise, etc.

Python package: inverted-encoding

We have released the Python 3 package “inverted-encoding” on PyPi (https://pypi.org/project/inverted-encoding/) and GitHub (https://github.com/paulscotti/inverted_encoding) for easy implementation of our eIEM procedure. The package contains two main functions, “IEM” and “permutation.”

For the “IEM” function, the only necessary inputs are an array of the stimulus features for every trial and a trial by voxel activations matrix (note: inputs other than voxels may be used for other modalities). The basis set can be specified as an optional parameter and will otherwise default to a basis set composed of nine equidistant channels each modeled as $\cos\left((\theta - \mu)\frac{\pi}{180}\right)^8$. The stimulus space defaults to a circular 0-179° range but can be optionally set to other ranges. Non-circular stimulus spaces can be set by the Boolean parameter “is_circular.” The IEM procedure defaults to a 10-fold cross-validation procedure but can be optionally specified. The final outputs are an array of each trial’s predicted stimulus, an array of each trial’s corresponding goodness-of-fit, each trial’s unaligned stimulus reconstruction, and each trial’s aligned stimulus reconstruction (aligned such that the correct stimulus is at zero in channel space). The user can then compute MAE themselves by averaging the (circular) absolute error between the predicted stimulus features and the actual stimulus features. We provide a convenience function, “circ_diff”, for computing circular error. The user can decide

whether they want to threshold any trials using the provided goodness-of-fit values prior to calculating MAE.

For the “permutation” function, the only necessary input is an array of the actual stimulus features. For each iteration, the stimulus features are randomly shuffled and used as the predicted stimuli to compute the MAE. The function outputs a null distribution of MAE values for the user to compare against the MAE obtained from the “IEM” function. A more exact and computationally intensive method would be to rerun the entire IEM pipeline with shuffled stimulus labels on every iteration to obtain the null distribution. This can also be performed using our package by simply repeating the IEM function with a different shuffling of the stimulus features for every iteration. Our exploratory comparisons of null distributions obtained using both approaches across the three fMRI datasets discussed in the main text yielded no obvious differences.

Data availability

The Perception dataset[48] is publicly available on OSF (https://osf.io/j7tpf/). The Memory dataset[43] is publicly available on OSF (https://osf.io/dkx6y). The Attention dataset[47] will be made publicly available upon final publication of the original study; researchers may contact the authors in the meantime.

Code availability

Code to implement eIEM is available as a Python package (https://pypi.org/project/inverted-encoding). Code to reproduce Figures 1 and 3 are available on OSF (https://osf.io/et7m2/).

Supplemental Information

An enhanced inverted encoding model for neural reconstructions

Paul S. Scotti, Jiageng Chen, & Julie D. Golomb

Table of Contents

Supplemental figures. 43

Supplemental table. 45

Supplemental references. 48

Supplemental figures.

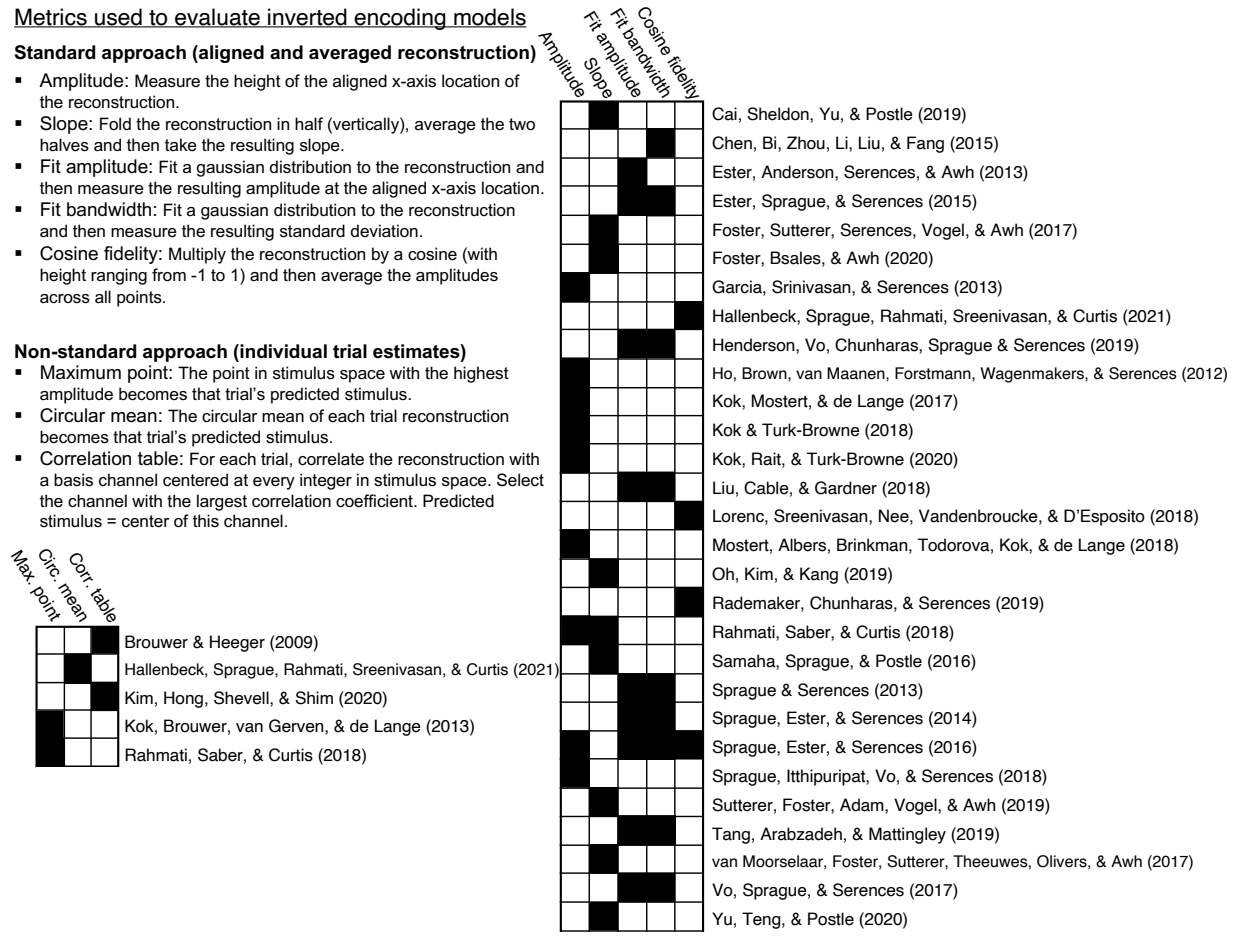

Supplemental Figure 4. Summary of metrics used to evaluate IEM reconstructions in a sampling of published paper[1–31]. Note that the methodological concerns raised in the Results apply to the metrics labeled under the standard approach, although our proposed modifications pose improvements over typical applications of the "maximum point", "circular mean", and "correlation table" approaches as well. The non-standard approaches can be quantified with a single value (like the standard approach metrics) by taking the mean absolute error between predicted and actual stimuli. Note that not all papers used the exact same procedure to obtain their listed IEM metric(s), and that the reader should investigate the individual papers of interest for more exact methodological details.

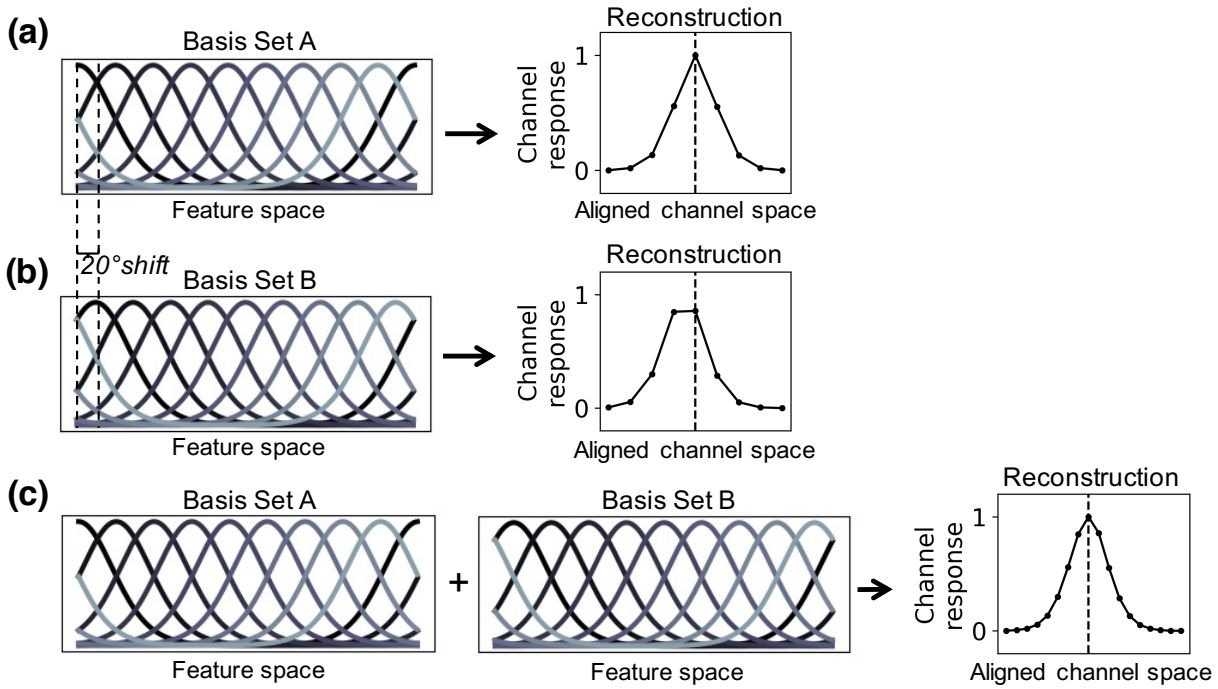

Supplemental Figure 5. Simulation depicting iterative shifting and its benefits for IEM reconstructions. The simulated neuroimaging data (trial by voxel activations) are identical for all three cases shown, and the underlying voxel tuning functions for this hypothetical brain region are known (simulated ground truth). The trial by voxel activations were constructed to reflect perfect (zero noise) information with identical train and test sets, such that the resulting reconstructions should also be perfect. (a) Basis set happens to perfectly reflect the underlying voxel tuning functions (simulated ground truth). (b) Reconstruction of the same data, now with a slightly altered basis set (channel means circularly shifted by 20°). Note that in a real experiment, the ground truth actual voxel tuning functions are not known, so the experimenter's arbitrary choice of channel centers could substantially alter resulting reconstructions, even if the same signal is present in all cases. This could result in misleading conclusions using the standard IEM technique. (c) By combining the results of both basis sets, the channel space changes from *num_channels* to *num_channels**2, leading to a fuller reconstruction. This is the principle of iterative shifting: In eIEM, we repeatedly fit the encoding model with every possible (circular) shift of the basis set (i.e. 1° shifts) and then combine all of these iterations together. This produces a fuller reconstruction that is no longer impoverished by a limited number of *num_channels* points (i.e., the range of channel space becomes equal to the range of stimulus space) and allows the correlation table metric to be optimally applied. This iterative shifting procedure also aids more generally in producing more interpretable and less biased reconstructions, as it allows our decoding model to be capable of predicting any possible feature in stimulus space (that is, not solely the stimuli that are located at the centers of the basis channels). Note that iterative shifting does not change the fact that different basis sets result in different reconstructions, rather, it simply allows for the most accurate reconstruction given a set number of channels with defined bandwidths.

Supplemental table.

Dataset	Procedure	Test description	T-stat	P-
Perception	IEM	V1	106.06	.000
		V4	53.33	.000
		IPS	27.70	.000
	eIEM	V1	-13.58	.000
		V4	-6.61	.000
		IPS	-5.12	.000
		V1 (5% excluded)	-13.73	.000
		V1 (10% excluded)	-15.79	.000
		V1 (25% excluded)	-22.06	.000
		V1 (50% excluded)	-29.65	.000
		V4 (5% excluded)	-7.11	.000
		V4 (10% excluded)	-7.97	.000
		V4 (25% excluded)	-9.18	.000
		V4 (50% excluded)	-13.63	.000
		IPS (5% excluded)	-5.54	.000
		IPS (10% excluded)	-5.86	.000
		IPS (25% excluded)	-6.78	.000
		IPS (50% excluded)	-8.54	.000
Attention	IEM	V1	16.02	.000
		V4	7.65	.001
		IPS	-0.16	.601
	eIEM	V1	-9.93	.000
		V4	-7.29	.000
		IPS	-0.11	.535
		V1 (5% excluded)	-9.64	.000
		V1 (10% excluded)	-9.79	.000
		V1 (25% excluded)	-10.08	.000
		V1 (50% excluded)	-11.49	.000
		V4 (5% excluded)	-7.36	.000
		V4 (10% excluded)	-7.42	.000
		V4 (25% excluded)	-7.88	.000
		V4 (50% excluded)	-7.86	.000
		IPS (5% excluded)	-1.15	.208
		IPS (10% excluded)	-1.06	.234
		IPS (25% excluded)	-0.87	.281
		IPS (50% excluded)	0.98	.842
	eIEM – brain-behavior	V1	7.02	.000
		V4	5.18	.002
		IPS	-1.06	.330
		V1 (5% excluded)	6.50	.001

		V1 (10% excluded)	6.30	.001
		V1 (25% excluded)	7.25	.000
		V1 (50% excluded)	6.69	.001
		V4 (5% excluded)	4.48	.003
		V4 (10% excluded)	4.81	.003
		V4 (25% excluded)	5.18	.002
		V4 (50% excluded)	7.03	.000
		IPS (5% excluded)	-0.85	.427
		IPS (10% excluded)	-1.38	.218
		IPS (25% excluded)	-0.70	.508
		IPS (50% excluded)	-0.41	.693
Memory	IEM – blank delay	V1	6.21	.001
		V4	6.38	.002
		IPS	4.70	.004
	IEM – distractor delay	V1	4.07	.008
		V4	5.55	.001
		IPS	5.57	.001
	IEM – blank vs. distractor	V1	4.18	.013
		V4	4.18	.011
		IPS	-0.53	.659
	eIEM – blank delay	V1	-4.88	.006
		V4	-5.79	.003
		IPS	-5.22	.005
		V1 (5% excluded)	-4.94	.006
		V1 (10% excluded)	-4.99	.006
		V1 (25% excluded)	-4.86	.006
		V1 (50% excluded)	-4.75	.007
		V4 (5% excluded)	-5.77	.003
		V4 (10% excluded)	-5.76	.003
		V4 (25% excluded)	-5.70	.003
		V4 (50% excluded)	-6.21	.002
		IPS (5% excluded)	-5.15	.005
		IPS (10% excluded)	-5.43	.004
		IPS (25% excluded)	-4.95	.006
		IPS (50% excluded)	-5.00	.006
	eIEM – distractor delay	V1	-4.07	.012
		V4	-4.26	.010
		IPS	-5.65	.002
		V1 (5% excluded)	-4.26	.010
		V1 (10% excluded)	-4.25	.010
		V1 (25% excluded)	-4.08	.012
		V1 (50% excluded)	-4.50	.008
		V4 (5% excluded)	-4.25	.010
		V4 (10% excluded)	-4.30	.010

		V4 (25% excluded)	-3.65	.019
		V4 (50% excluded)	-4.09	.012
		IPS (5% excluded)	-5.18	.005
		IPS (10% excluded)	-5.35	.004
		IPS (25% excluded)	-5.92	.002
		IPS (50% excluded)	-6.11	.001
	eIEM – blank vs. distractor	V1	-7.55	.000
		V4	-2.85	.049
		IPS	-3.03	.041
		V1 (5% excluded)	-7.14	.001
		V1 (10% excluded)	-7.08	.001
		V1 (25% excluded)	-9.32	.000
		V1 (50% excluded)	-2.73	.056
		V4 (5% excluded)	-2.89	.048
		V4 (10% excluded)	-3.13	.038
		V4 (25% excluded)	-6.21	.019
		V4 (50% excluded)	-3.57	.021
		IPS (5% excluded)	-2.68	.060
		IPS (10% excluded)	-2.48	.076
		IPS (25% excluded)	-0.94	.437
		IPS (50% excluded)	0.20	.862

Supplemental Table 1. Statistics from tests depicted in Figure 2 from the main text.

Supplemental references.

1. Cai, Y., Sheldon, A. D., Yu, Q. & Postle, B. R. Overlapping and distinct contributions of stimulus location and of spatial context to nonspatial visual short-term memory. *Journal of neurophysiology* **121**, 1222–1231 (2019).
2. Chen, N. *et al.* Sharpened cortical tuning and enhanced cortico-cortical communication contribute to the long-term neural mechanisms of visual motion perceptual learning. *Neuroimage* **115**, 17–29 (2015).
3. Ester, E. F., Anderson, D. E., Serences, J. T. & Awh, E. A neural measure of precision in visual working memory. *Journal of cognitive neuroscience* **25**, 754–761 (2013).
4. Ester, E. F., Sprague, T. C. & Serences, J. T. Parietal and frontal cortex encode stimulus-specific mnemonic representations during visual working memory. *Neuron* **87**, 893–905 (2015).
5. Foster, J. J., Sutterer, D. W., Serences, J. T., Vogel, E. K. & Awh, E. Alpha-band oscillations enable spatially and temporally resolved tracking of covert spatial attention. *Psychological science* **28**, 929–941 (2017).
6. Foster, J. J., Bsales, E. M. & Awh, E. Covert spatial attention speeds target individuation. *Journal of Neuroscience* **40**, 2717–2726 (2020).
7. Garcia, J. O., Srinivasan, R. & Serences, J. T. Near-real-time feature-selective modulations in human cortex. *Current Biology* **23**, 515–522 (2013).
8. Hallenbeck, G. E., Sprague, T. C., Rahmati, M., Sreenivasan, K. K. & Curtis, C. E. Working memory representations in visual cortex mediate distraction effects. *Nat Commun* **12**, 4714 (2021).

9. Henderson, M., Vo, V., Chunharas, C., Sprague, T. & Serences, J. Multivariate analysis of BOLD activation patterns recovers graded depth representations in human visual and parietal cortex. *Eneuro* **6**, (2019).
10. Ho, T. *et al.* The optimality of sensory processing during the speed–accuracy tradeoff. *Journal of Neuroscience* **32**, 7992–8003 (2012).
11. Kim, I., Hong, S. W., Shevell, S. K. & Shim, W. M. Neural representations of perceptual color experience in the human ventral visual pathway. *Proceedings of the National Academy of Sciences* **117**, 13145–13150 (2020).
12. Kok, P. & Turk-Browne, N. B. Associative prediction of visual shape in the hippocampus. *Journal of Neuroscience* **38**, 6888–6899 (2018).
13. Kok, P., Brouwer, G. J., van Gerven, M. A. & de Lange, F. P. Prior expectations bias sensory representations in visual cortex. *Journal of Neuroscience* **33**, 16275–16284 (2013).
14. Kok, P., Mostert, P. & De Lange, F. P. Prior expectations induce prestimulus sensory templates. *Proceedings of the National Academy of Sciences* **114**, 10473–10478 (2017).
15. Kok, P., Rait, L. I. & Turk-Browne, N. B. Content-based dissociation of hippocampal involvement in prediction. *Journal of Cognitive Neuroscience* **32**, 527–545 (2020).
16. Liu, T., Cable, D. & Gardner, J. L. Inverted encoding models of human population response conflate noise and neural tuning width. *Journal of Neuroscience* **38**, 398–408 (2018).

17. Lorenc, E. S., Sreenivasan, K. K., Nee, D. E., Vandenbroucke, A. R. & D'Esposito, M. Flexible coding of visual working memory representations during distraction. *Journal of Neuroscience* **38**, 5267–5276 (2018).
18. Mostert, P. *et al.* Eye movement-related confounds in neural decoding of visual working memory representations. *Eneuro* **5**, (2018).
19. Oh, B.-I., Kim, Y.-J. & Kang, M.-S. Ensemble representations reveal distinct neural coding of visual working memory. *Nature communications* **10**, 1–12 (2019).
20. Rademaker, R. L., Chunharas, C. & Serences, J. T. Coexisting representations of sensory and mnemonic information in human visual cortex. *Nature neuroscience* **22**, 1336–1344 (2019).
21. Rahmati, M., Saber, G. T. & Curtis, C. E. Population Dynamics of Early Visual Cortex during Working Memory. *Journal of Cognitive Neuroscience* **30**, 219–233 (2018).
22. Samaha, J., Sprague, T. C. & Postle, B. R. Decoding and reconstructing the focus of spatial attention from the topography of alpha-band oscillations. *Journal of cognitive neuroscience* **28**, 1090–1097 (2016).
23. Sprague, T. C. & Serences, J. T. Attention modulates spatial priority maps in the human occipital, parietal and frontal cortices. *Nature neuroscience* **16**, 1879–1887 (2013).
24. Sprague, T. C., Ester, E. F. & Serences, J. T. Reconstructions of information in visual spatial working memory degrade with memory load. *Current Biology* **24**, 2174–2180 (2014).

25. Sprague, T. C., Ester, E. F. & Serences, J. T. Restoring latent visual working memory representations in human cortex. *Neuron* **91**, 694–707 (2016).
26. Sprague, T. C., Itthipuripat, S., Vo, V. A. & Serences, J. T. Dissociable signatures of visual salience and behavioral relevance across attentional priority maps in human cortex. *Journal of neurophysiology* **119**, 2153–2165 (2018).
27. Sutterer, D. W., Foster, J. J., Adam, K. C., Vogel, E. K. & Awh, E. Item-specific delay activity demonstrates concurrent storage of multiple active neural representations in working memory. *PLoS biology* **17**, e3000239 (2019).
28. Tang, M. F., Arabzadeh, E. & Mattingley, J. B. Forward modelling reveals dynamics of neural orientation tuning to unconscious visual stimuli during binocular rivalry. *bioRxiv* (2019) doi:10.1101/574905.
29. Van Moorselaar, D. *et al.* Spatially selective alpha oscillations reveal moment-by-moment trade-offs between working memory and attention. *Journal of cognitive neuroscience* **30**, 256–266 (2018).
30. Vo, V. A., Sprague, T. C. & Serences, J. T. Spatial tuning shifts increase the discriminability and fidelity of population codes in visual cortex. *Journal of Neuroscience* **37**, 3386–3401 (2017).
31. Yu, Q., Teng, C. & Postle, B. R. Different states of priority recruit different neural representations in visual working memory. *PLoS biology* **18**, e3000769 (2020).